

See discussions, stats, and author profiles for this publication at: <https://www.researchgate.net/publication/265905796>

Mass Spectrometry and Imaging Analysis of Nanoparticle-Containing Vesicles Provide a Mechanistic Insight into Cellular Trafficking

ARTICLE in ACS NANO · SEPTEMBER 2014

Impact Factor: 12.88 · DOI: 10.1021/nn502754c

CITATIONS

6

READS

163

8 AUTHORS, INCLUDING:



[Stefan Tenzer](#)

Johannes Gutenberg-Universität Mainz

102 PUBLICATIONS 2,135 CITATIONS

[SEE PROFILE](#)



[Hansjörg Schild](#)

Johannes Gutenberg-Universität Mainz

208 PUBLICATIONS 13,617 CITATIONS

[SEE PROFILE](#)



[Katharina Landfester](#)

Max Planck Institute for Polymer Research

597 PUBLICATIONS 14,129 CITATIONS

[SEE PROFILE](#)



[Volker Mailänder](#)

Universitätsmedizin der Johannes Gutenber...

125 PUBLICATIONS 3,580 CITATIONS

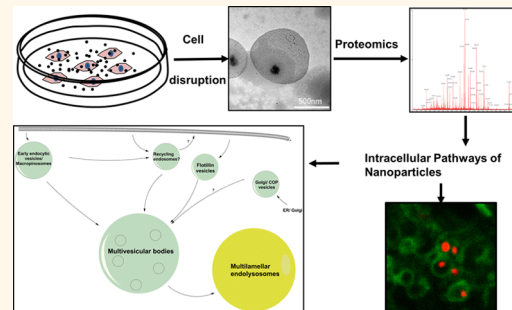
[SEE PROFILE](#)

Mass Spectrometry and Imaging Analysis of Nanoparticle-Containing Vesicles Provide a Mechanistic Insight into Cellular Trafficking

Daniel Hofmann,^{†,‡} Stefan Tenzer,[§] Markus B. Bannwarth,^{†,§} Claudia Messerschmidt,[†] Simone-Franziska Glaser,[†] Hansjörg Schild,[§] Katharina Landfester,[†] and Volker Mailänder^{*,†,‡}

[†]Max Planck Institute for Polymer Research, Ackermannweg 10, 55128 Mainz, Germany, [‡]Department of Medicine III, Hematology, Oncology and Pneumology, University Medical Center of the Johannes Gutenberg University Mainz, Langenbeckstrasse 1, 55101 Mainz, Germany, [§]Institute for Immunology, University Medical Center of the Johannes Gutenberg University Mainz, Langenbeckstrasse 1, 55101 Mainz, Germany, and [†]Graduate School Materials Science in Mainz, Staudinger Weg 9, 55128 Mainz, Germany

ABSTRACT Rational design of nanocarriers for drug delivery approaches requires an unbiased knowledge of uptake mechanisms and intracellular trafficking pathways. Here we dissected these processes using a quantitative proteomics approach. We isolated intracellular vesicles containing superparamagnetic iron oxide polystyrene nanoparticles and analyzed their protein composition by label-free quantitative mass spectrometry. The proteomic snapshot of organelle marker proteins revealed that an atypical macropinocytic-like mechanism mediated the entry of nanoparticles. We show that the entry mechanism is controlled by actin reorganization, atypical macropinocytic signaling, and ADP-ribosylation factor 1. Additionally, our proteomics data demonstrated a central role for multivesicular bodies and multilamellar lysosomes in trafficking and final nanoparticle storage. This was confirmed by confocal microscopy and cryo-TEM measurements. By quantitatively analyzing the protein composition of nanoparticle-containing vesicles, our study clearly defines the routes of nanoparticle entry, intracellular trafficking, and the proteomic milieu of a nanoparticle-containing vesicle.



KEYWORDS: nanoparticles · magnetic purification · vesicles · endosomes · intracellular trafficking · multivesicular bodies · multilamellar lysosomes · macropinocytosis-like · endocytosis

Recent studies have intensively analyzed the composition of the protein corona formed on nanoparticles after their contact with blood plasma.^{1–4} Going beyond this, our recent study aimed to use proteomics to characterize the milieu of nanoparticle-containing vesicles during their uptake and intracellular trafficking.^{5,6} These are very dynamic processes with a rapidly changing proteomic environment.^{7–10} During intracellular trafficking, homotypic as well as heterotypic fusion events and maturation processes drastically change the identity of the distinct endocytic vesicles.^{7,10–13} The fast conversion of endosomal marker proteins, as well as the lively crosstalk of endocytic vesicles with the trans-Golgi-network (TGN) and the autophagic pathway, challenges the investigation of intracellular nanoparticle trafficking.^{7,14–16} Here it is

important to mention that a large number of previous studies already roughly elucidated the trafficking of distinct nanoparticles.^{13,17–19} Several investigations show that the majority of nanoparticles are transported to lysosomes, while some others are recycled to the cell membrane by endosomes or undergo other ways of exocytosis.^{13,20–22} Since the transitions of these intracellular trafficking pathways frequently are smoothly blending with uptake mechanisms, it appears to be mandatory to perform a combined study investigating intracellular trafficking and uptake mechanisms at the same time. This guarantees to obtain novel information about participating proteins.^{23,24} These include proteins (e.g., ARF1, Rab5) which participate during the entry and the intracellular trafficking pathways.^{24–27} Moreover, the so far

* Address correspondence to mailander@mpip-mainz.mpg.de.

Received for review May 20, 2014 and accepted September 22, 2014.

Published online
10.1021/nn502754c

© XXXX American Chemical Society

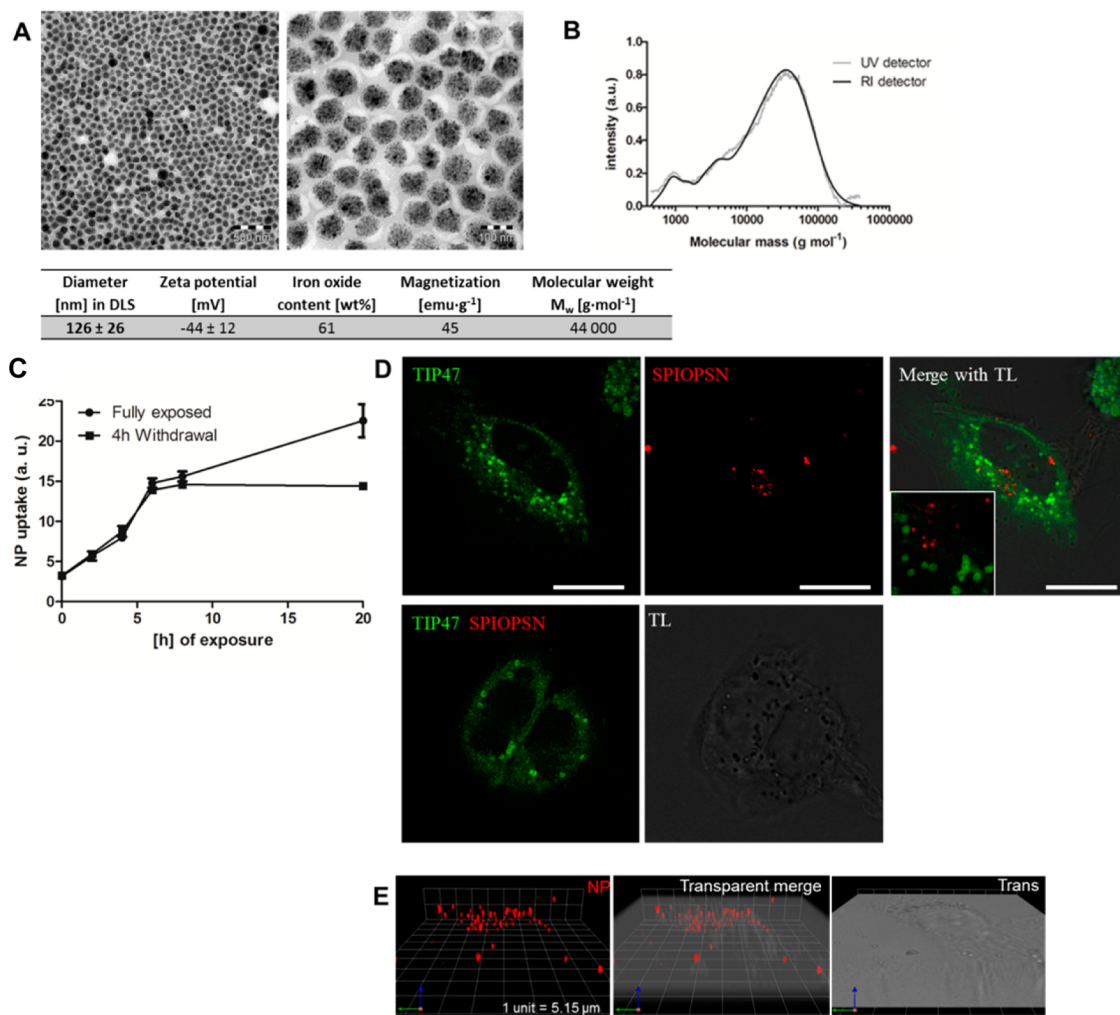


Figure 1. Characterization of nanoparticles. (A) Transmission electron microscopy images of SPIOPSN illustrated the homogeneous distribution of iron oxide nanoparticles among the polystyrene nanoparticles with an average rate of about 61 wt % as determined by thermogravimetric analysis. Transmission electron microscopy and dynamic light scattering revealed an average size distribution of 126 nm. The ~10 nm sized superparamagnetic iron oxide nanoparticles showed a homogeneous distribution inside the polystyrene matrix. SPIOPSN possessed a high saturation magnetization of 45 emu g^{-1} . (B) Size exclusion chromatography (SEC) simultaneously detected fluorescent dye (UV) and polystyrene (RI). Size exclusion chromatography confirmed the exclusion of free dye in our nanoparticle dispersion. (C) The measurement of uptake kinetics carried out by flow cytometry displayed a rapid uptake of SPIOPSN up to 20 h. In the second measurement, nanoparticles were withdrawn after 4 h. The nanoparticle content remains stable from this time point, hereby excluding exocytosis. (D) The fluorescent dye does not dissociate from the nanoparticles. Since free BODIPY is transported to lipid droplets, we counterstained cells with TIP47.⁵⁶ The 150 $\mu\text{g mL}^{-1}$ nanoparticles and nanoparticle supernatant (lower two panels) were checked for free dye molecules. No colocalization was observed (scale bar 5 μm). (E) SPIOPSN were mostly taken up linearly and widely distributed through the cell as shown by confocal laser scanning microscopy. The panels depict a homogeneous intracellular distribution of the magnetic nanoparticles (20 h, 150 $\mu\text{g mL}^{-1}$, 1 unit = 5.15 μm).

unknown hydrolytic proteins of nanoparticle-containing lysosomes are of great interest since this knowledge could be utilized to more efficiently design nanomaterials for drug delivery approaches. This knowledge could aid to improve the process of nanomaterial disassembly, drug release and the degradation of the nanoparticulate protein corona.^{28,29}

RESULTS AND DISCUSSION

To analyze the uptake mechanisms, the intracellular nanoparticle trafficking and the proteomic compositions of SPIOPSN-containing vesicles, we chose HeLa and human mesenchymal stem cells (MSC) as model

systems. HeLa cells as malignant cell line are widely used in the field, while MSC are primary cells interesting in regenerative therapy. Incubation of HeLa and human mesenchymal stem cells with fluorescently labeled superparamagnetic iron oxide polystyrene nanoparticles (SPIOPSN, for characterization see Figure 1A,B) showed a continuous internalization of nanoparticles over 20 h (Figure 1C). Therefore, we chose 20 h for proteomic analysis because a significant amount of nanoparticles was found in the final cell designation, the multilamellar lysosomes, while others were just internalized into newly formed endocytic vesicles. Morphologically, SPIOPSN were transported

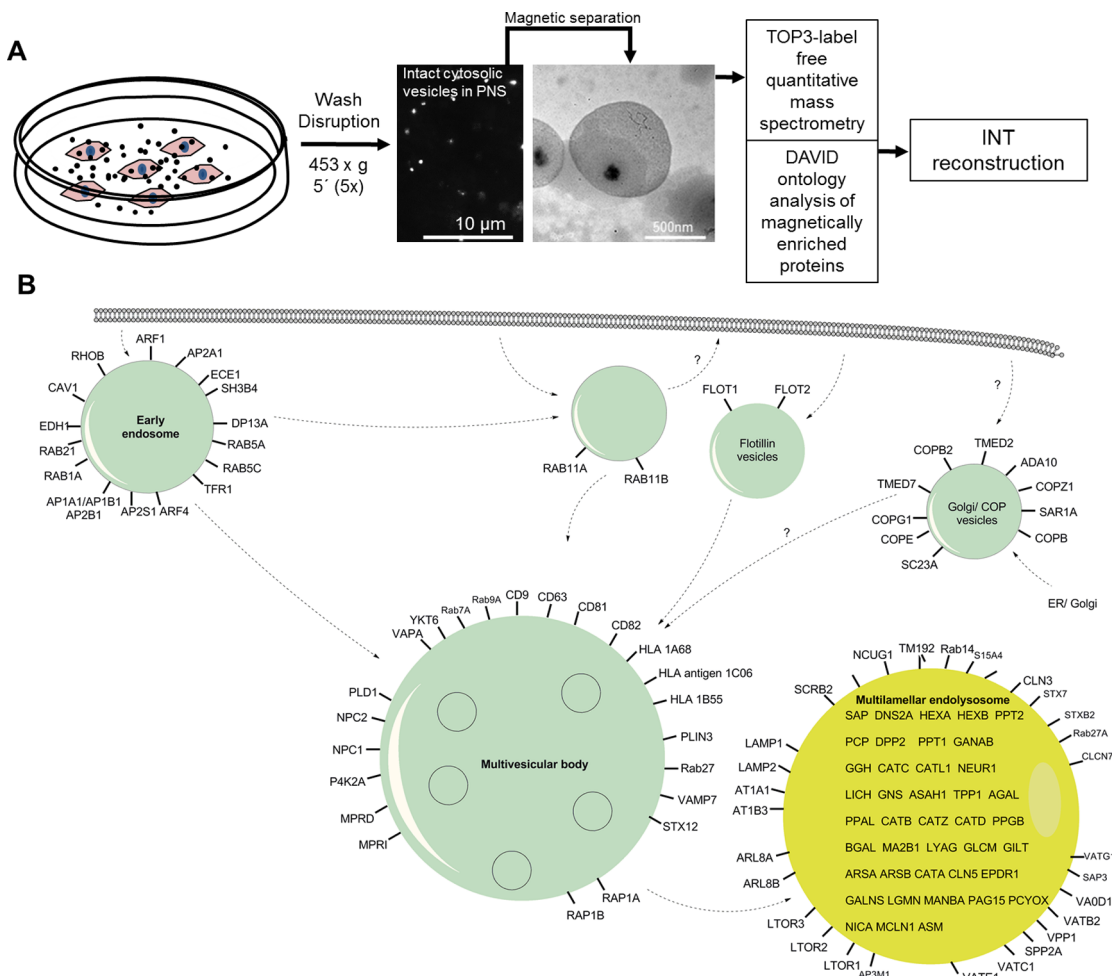


Figure 2. Reconstruction of intracellular nanoparticle trafficking. (A) After 20 h of SPIOPSN incubation and extensive washing, HeLa cells were disrupted, debris was removed, and intact vesicles were prepared for label-free quantitative mass spectrometry. (B) After DAVID ontology analysis, intracellular nanoparticle trafficking was reconstructed based on GOTERMs *vesicle* and *lysosome*. Subcellular classification of identified proteins is based on the proteins that were magnetically enriched by a factor of >2-fold. Reconstruction of intracellular nanoparticle trafficking is schematically illustrated. Protein names are depicted by their Uniprot IDs.

inside roundly shaped vesicles in a size range of 500–1000 nm (Supporting Information Figure S1C). Furthermore, we found no significant signs of dye leakage (Figure 1D, Supporting Information Figure S1D), cytotoxicity (Supporting Information Figure S1A,B) or nanoparticle exocytosis (Figure 1C) after this time.

Dissection of Intracellular Nanoparticle Trafficking by Proteomic Snapshot Analysis. We used the superparamagnetic features of SPIOPSN to magnetically isolate intracellular nanoparticle-containing vesicles from HeLa cells after 20 h of nanoparticle exposure. Transmission electron microscopy confirmed the presence of a large number of NP-containing vesicles inside the magnetically enriched fraction (Figure 2A). Next, we determined the proteomic composition of these vesicles using a TOP3-based label-free quantitative mass spectrometry approach.³⁰ Overall, we were able to identify and quantify 1492 proteins in the magnetically enriched fraction; of those, 884 were found to be enriched by a factor of at least 2 relative to

the nonmagnetic fraction (Supporting Information Tables S1–S6). Then, we applied DAVID protein ontology analysis to identify potential uptake pathways and intracellular nanoparticle trafficking pathways *in silico* (Supporting Information Table S1).³¹ For dissection of the intracellular trafficking pathways, we used the GOTERMs *lysosome* and *vesicle* (Supporting Information Tables S2 and S3).

Uptake Mechanisms: Markers of Macropinosomes and Early Endosomal Proteins Were Identified on SPIOPSN-Containing Vesicles. Next, we subcategorized the identified proteins according to their known subcellular localization in literature (Figure 2B). Confirmatory for our approach, we identified early endocytic proteins such as RAB5A and RAB5C. Additionally, live cell imaging demonstrated an active transport of SPIOPSN inside Rab5A⁺ vesicles (Supporting Information Figure S2). We also identified RhoB, which has been associated with the (macro)pinocytic machinery.³² Interestingly, RhoB and Rab5A⁺ NP-containing vesicles were both visible by

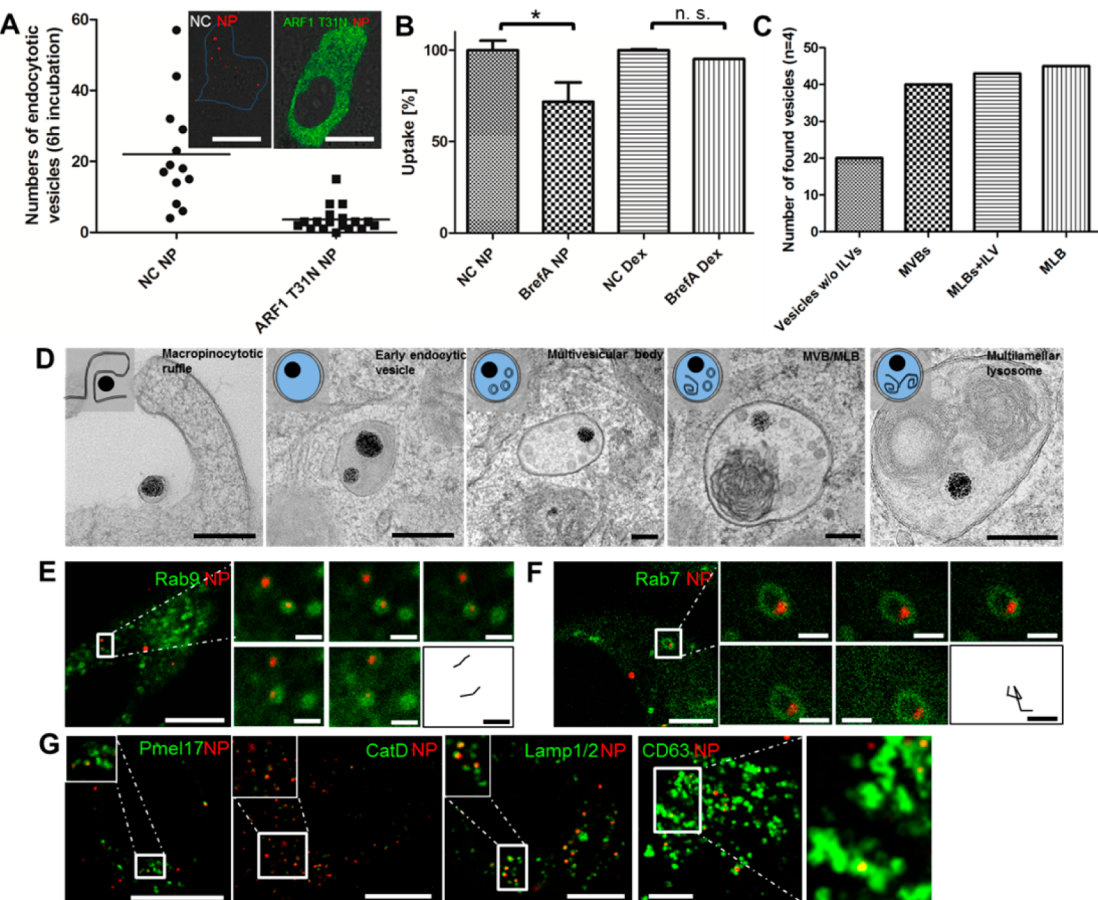


Figure 3. Intracellular trafficking of SPIOPSN. (A) Twenty-four hours after transfection of HeLa cells with ARF1 T31N DN, $150 \mu\text{g mL}^{-1}$ SPIOPSN were added for 6 h ($***p < 0.001$). Number of SPIOPSN-containing vesicles was quantitatively determined by the analysis of z-stacks. (B) HeLa cells were pretreated with $10 \mu\text{g mL}^{-1}$ Brefeldin A followed by a 5 h incubation of $150 \mu\text{g mL}^{-1}$ SPIOPSN ($*p < 0.01$). SPIOPSN uptake was quantitatively analyzed by flow cytometry. (C) Quantitative analysis of TEM micrographs. Vesicles were classified owing to the morphological criteria as shown in the sketches of (D). Abundance of different endolysosomal compartments after 20 h of SPIOPSN incubation ($n = 4$ independent experiments). (D) SPIOPSN entered HeLa cells via macropinocytic ruffles. Transport to multilamellar lysosomes via multivesicular bodies containing intraluminal vesicles. Multilamellar lysosomes contained wrapped lipid bilayers. (E and F) Trafficking of SPIOPSN was observed along Rab9⁺ and Rab7⁺ vesicles. (G) Pmel17 and CD63 colocalized with SPIOPSN after 6 h of exposure. SPIOPSN end up in Cathepsin D⁺ and Lamp1/2⁺ multilamellar lysosomes after 20 h of exposure (scale bar cLSM, $5 \mu\text{m}$; magnification, $1 \mu\text{m}$; scale bar TEM, 200 nm).

differential interference contrast (DIC) microscopy and resembled fluid-phase filled macropinosomes (Supporting Information Figure S2).²⁴ Another protein that was associated with macropinocytic mechanisms was the identified ADP-ribosylation factor 1 (ARF1).³³ Hasegawa *et al.* demonstrated that the overexpression of dominant negative ARF1 T31N induced an incomplete closure of the circular dorsal ruffles hereby blocking the macropinocytic uptake mechanism in an ARF1-dependent manner.³³ After the overexpression of dominant negative ARF1, we recorded only less colocalization with SPIOPSN (Supporting Information Figure S2). However, we observed that ARF1 T31N (DN) cells displayed a very low number of internalized nanoparticles (Figure 3A). We observed that ARF1 T31N had a significant effect on the uptake rate of nanoparticles. This was also confirmed by the pharmacological inhibition of ARF1 by Brefeldin A (Figure 3B)

indicating that ARF1 plays a major role during the macropinocytic-like entry of SPIOPSN.

To verify additional proteins that participate during the early stages of SPIOPSN entry, we overexpressed SWAP70-GFP, Rac1-Q61L-GFP, cdc42-Q61L-GFP and cdc42-T17N-GFP as markers for macropinocytic ruffles and macropinosomes. Fluorescence microscopy imaging indicated no colocalization of SWAP70 with SPIOPSN, but identified SPIOPSN inside Rac1 positive vesicular compartments (Figure 4E,F). These vesicles resembled nonbudded premacropinosomes that were filled with SPIOPSN.³⁴ A similar phenotype was observed during the overexpression of cdc42-Q61L-GFP, where we found SPIOPSN inside roundly shaped premacropinosomes (Supporting Information Figure S2). As confirmation, the presence of cdc42 in magnetically isolated SPIOPSN-containing vesicles was also shown by mass spectrometry (Supporting Information Table S4).

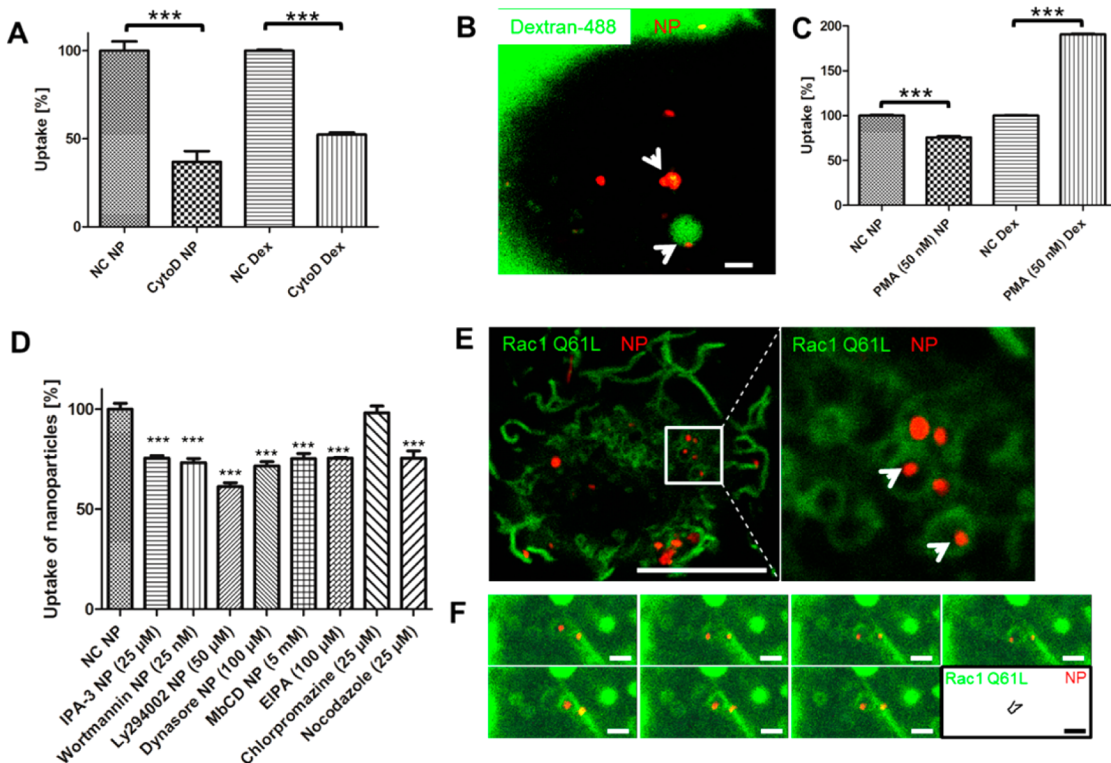


Figure 4. SPIOPSN are mainly internalized *via* a dynamin-dependent macropinocytosis-like mechanism. (A) SPIOPSN ($150 \mu\text{g mL}^{-1}$) were incubated with cytochalasin D ($150 \mu\text{M}$) pretreated HeLa cells to investigate the effect of inhibition of F-Actin polymerization. Ten kilodalton AF488-Dextran served as a control. Values are given as mean \pm SD ($n = 3$ independent experiments); *** $p < 0.001$. (B) Localization of SPIOPSN and 10 kDa AF488-Dextran during a co-internalization experiment (white arrows indicate sites of colocalization; scale bar $1 \mu\text{m}$). (C) HeLa cells were prestimulated for 45 min with 50 nM phorbol myristate acetate (PMA) and incubated with SPIOPSN and 10 kDa AF488-Dextran. Experiments were performed in triplicates; errors are plotted as median \pm SD; *** $p < 0.001$. (D) HeLa cells were preincubated with multiple small molecules that partially inhibited SPIOPSN internalization (*** $p < 0.001$ except for the inhibition by chlorpromazine). (E) Confocal microscopy of cells exposed to SPIOPSN (6 h) in a Rac1-Q61L-GFP positive cell (scale bar $= 10 \mu\text{m}$). (F) A snapshot of vesicular tracks shows the movement of SPIOPSN in a Rac1-Q61L-GFP $^{+}$ vesicle. Images were recorded every 3 s (scale bar $= 1 \mu\text{m}$). A motility profile of the nanoparticle was generated.

Entry of Nanoparticles into the Endocytic System Is Mediated by a Macropinocytic-like Mechanism. Our previous experiments showed that nanoparticles were internalized *via* macropinosome-like organelles. Next, we further investigated the nanoparticle entry mechanisms by the use of different membrane permeable inhibitor molecules that affect macropinocytic signaling pathways. Since macropinocytosis depends on the reorganization of actin, we initially focused on the modulation of actin cytoskeleton.^{23,35,36}

We found that the uptake of SPIOPSN was mainly suppressed by F-actin inhibition (Figure 4A), whereas myosin II inhibition had no effect on cellular uptake (Supporting Information Figure S3). Most of the nanoparticles colocalized with the fluid phase marker dextran (10 kDa) after 4–6 h of incubation inside smaller and larger endocytic structures (Figure 4B). Our multiple inhibitor studies revealed that vesicle uptake is mainly affected by key players of the macropinocytic system.³⁷ Relative to control experiments, we observed a reduced number of internalized nanoparticles after the treatment of cells with a PAK1 inhibitor (IPA3) and two classical inhibitors of PI3K (Wortmannin and

Ly294002).^{38,39} EIPA, a macropinocytic inhibitor, reduced the uptake of nanoparticles (Figure 4D).⁴⁰ Moreover, nocodazole significantly inhibited SPIOPSN uptake.⁴¹ Interestingly, while the inhibition of PKC (7 mM Ro 31-8220) and PLC (10 μM U-73122) had no effect on SPIOPSN uptake (data not shown),³⁹ the stimulation of PKC signaling by phorbol myristate acetate (PMA) and EGF led to a decrease in SPIOPSN uptake but to an increase in fluid-phase dextran uptake displaying a size limitation for SPIOPSN in PMA-stimulated pinocytosis (Figure 4C and Supporting Information Figure S3).⁴² We also observed a reduction of SPIOPSN uptake after dynasore treatment and the overexpression of dynamin2 K44A indicating that dynamin2 mediates SPIOPSN entry (Supporting Information Figure S4). This strengthens the role for dynamin2 in a macropinocytic-like uptake mechanism. On a subcellular level, it is known that dynamin participates in the formation of macropinocytic protrusions.⁴³ Schlunck and colleagues showed that the disruption of Dynamin2 leads to an altered Rac localization from the cell edges into abnormal dorsal ruffles leading to a decrease of lamellipodia formation.⁴³

To exclude a role for dynamin in clathrin or caveolae-mediated uptake, we showed that the treatment with clathrin uptake inhibitor chlorpromazine, as well as the overexpression of Epsin DIII and caveolin 1, did not alter the uptake of nanoparticles (Figure 4D/ Supporting Information Figure S4). siRNA-mediated knockdown showed that the uptake of SPIOPSN was neither mediated by clathrin heavy chain nor by caveolin-1 (Supporting Information Figure S4D,E). Altogether, we observed that SPIOPSN are internalized *via* an atypical macropinocytic mechanism, which further interplays with the endolysosomal trafficking system.

Intracellular Trafficking: Proteins of SPIOPSN-Containing Multivesicular Bodies. After entry, we were able to identify nanoparticles inside intracellular compartments connecting early endocytic compartments with lysosomal compartments. As prominent markers for multivesicular bodies, we identified RAB7A, RAB9A and VAMP7 by mass spectrometry.^{16,44,45} Also in live cell imaging experiments, we observed a colocalization of SPIOPSN with RAB7A, RAB9A and VAMP7 positive endosomes that actively trafficked through the cell (Figure 2B, Figure 3E,F and Supporting Information Figure S5).⁴⁴

Additionally, MVBs harbor several tetraspanins (*e.g.*, CD9, CD63, CD81, CD82) and HLA molecules (*e.g.*, HLA MHC class I antigen A*68) inside their membrane (Figure 2B). For CD63, we confirmed the colocalization with SPIOPSN by immunofluorescence stainings indicating that nanoparticles are in close proximity to intraluminal vesicles (Figure 3).⁴⁶ Previous studies showed a CD63-dependent sorting of Pmel17 into intraluminal vesicles of MVBs.⁴⁶ Since we observed a colocalization of SPIOPSN with CD63, we asked whether Pmel17 is sorted into SPIOPSN-containing vesicles. We overexpressed Pmel17, a melanosomal protein located in intraluminal vesicles inside MVBs.^{46,47} Indeed, colocalization indicated that nanoparticles are in close proximity to the neighboring intraluminal vesicles (Figure 3). We confirmed the localization of SPIOPSN inside MVBs by cryo-TEM experiments (Figure 3C,D). The analysis of TEM images displayed that SPIOPSN are shuttled *via* ILV-enriched multivesicular bodies to multilamellar lysosomes containing characteristic membrane whorls (Figure 3C). After 20 h, a large number of nanoparticles was stored inside the terminal multilamellar lysosomes.

RNAi-mediated knockdown of the tetraspanin CD81 significantly reduced the uptake of SPIOPSN (Supporting Information Figure S4). In this context it was previously shown that CD81 regulates the formation of lamellipodia.⁴⁸ In dendritic cells, CD81 knockdown subsequently lowers the activity of Rac1 in an actin-dependent fashion.⁴⁸ Therefore, we concluded that CD81 is involved in the macropinocytic-like uptake mechanism of SPIOPSN.

Further proteins of MVBs that were identified by mass spectrometry are the cholesterol transporters Niemann Pick disease C1 (NPC1) and Niemann Pick disease C2 (NPC2).⁴⁹ Previous reports showed that the depletion of NPC1 leads to endolysosomal dysfunction and disturbance of intracellular transporting processes owing to defects in cholesterol transport.²⁰ Therefore, we focused on the effect of cholesterol on the entry of SPIOPSN. First, we found that cholesterol depletion by methyl- β -cyclodextrin significantly inhibited the uptake of SPIOPSN (Figure 4D). To mimic the phenotype of NPC1-depleted cells, we used the cholesterol synthesis inhibitor U18666A. The accumulation of cholesterol inside the endolysosomal system significantly decreased uptake of SPIOPSN and dextran revealing an important role for cholesterol homeostasis in SPIOPSN entry (Supporting Information Figure S4F).

Intracellular Storage: Lysosomal Membrane Proteins Identified by MS. While other studies rely on colocalization studies with a single lysosomal marker or a fluorescent labeling of endosomes with a low pH, we found a wide range of proteins associated with the lysosomal compartment (Figure 2B; Supporting Information Table S2). Confirmatory to the literature, LAMP1 and LAMP2 were identified by MS. Intracellular immunofluorescence (IF) staining validated that LAMP1 and LAMP2 were associated with SPIOPSN-containing vesicles (Figure 3G). Further on, cathepsins as well as other characteristic lysosomal matrix proteins (*e.g.*, hydrolases, galactosidases and thioesterases) were identified (Figure 2B; see proteins in the reconstruction of multilamellar lysosomes; Supporting Information Tables S2 and S3). IF stainings showed a high rate of SPIOPSN colocalization with cathepsin D in HeLa cells and in human mesenchymal stem cells (Figure 3G; Supporting Information Figure S6). The hydrolytic potential of the nanoparticle-containing lysosomes was shown as we observed a degradation of the nanoparticle-associated protein corona inside lysosomes. We demonstrated that the protein corona is taken up into the endolysosomal system but is then degraded inside Lamp1⁺/Lamp2⁺ lysosomal organelles (Supporting Information Figure S7).

At the same time, we were also able to identify several v-type proton ATPase pumps that are known to obtain the lysosomal pH (*e.g.*, VATG1, VATC1) (Figure 2B). Inhibition of v-type ATPases by Bafilomycin A1 drastically decreased SPIOPSN uptake. Consequently, we concluded that the functionality of v-type proton ATPase pumps is required for the macropinocytic-like uptake mechanism (Supporting Information Figure S3).

Other Relevant Proteins That Were Identified by MS. Other proteins such as flotillin 1 (FLOT1) and flotillin 2 (FLOT2) were identified (Figure 2B).⁵⁰ In RNAi-mediated experiments, we observed a decreased endocytosis of SPIOPSN after siRNA mediated knockdown of

flotillin-1 (Supporting Information Figure S4E).⁵¹ Therefore, we concluded that flotillin-1 is not only present in MVBs but fulfills also tasks during the uptake of SPIOPSN. Next, we analyzed whether proteins of the recycling pathways were associated with SPIOPSN-containing vesicles. Indeed, RAB11A and RAB11B were enriched in the magnetic fraction. However, in live cell imaging, less colocalization of nanoparticles with Rab11 (data not shown) was observed.¹³ Therefore, we concluded that SPIOPSN were not exocytosed via the recycling pathway. This was also confirmed by pulse experiments, where no significant drop of internalized nanoparticles was observed over time (Figure 1C). It is important to mention that Rab11 is not only a marker for recycling endosomes but is also present onto early endocytic vesicles and MVBs, which has to be considered when investigating nanoparticle trafficking.^{11,12}

Identification of Proteins Heavily Depends on the Method of Subcellular Fractionation. Subcellular fractionation methods are prone to impurities inside the sample, leading to the detection of contaminating proteins, especially when highly sensitive MS methods are used.⁵² This poses stringent requirements on subcellular fractionation protocols, especially for the preparation of endosomal compartments. Notably, even highly “pure” endosomal fractions always contain proteins from other compartments, since the cell uses the endocytic pathway for the degradation of nonendolysosomal constituents.⁵³ Especially, the fusion of autophagosomes with lysosomes may insert impurities of defect organelles such as mitochondria or other damaged vesicles.⁵³ This was also shown by our experiments, where we identified large membrane whorls inside the endolysosomal structures, which at the same time harbored magnetic nanoparticles (the last two panels of Figure 3D). DAVID ontology analysis of the remaining nonendolysosomal proteins revealed an enrichment of markers of the cytoskeleton (~26) and the pore complex (~6) (Supporting Information Table S6). To reliably distinguish between positive and false positive results, analyzing the enrichment of proteins in the purified fraction relative to the remaining fraction is mandatory. False negative results may be caused by low abundance of the proteins in the investigated fraction or degradative processes. Additionally, low copy number proteins as well as small proteins (e.g., subunits), hydrophobic insoluble transmembrane proteins, proteins with post-translational modifications and loosely attached proteins may be

hard to detect.⁵² While these restrictions may limit interpretation of the data, the quantitative analysis of vesicular proteins by MS is a valuable tool to screen for new components of the nanoparticle uptake and trafficking machinery.

CONCLUSIONS

Overall, we utilized a novel approach with label-free quantitative mass spectrometry to analyze uptake mechanisms and intracellular nanoparticle transport after a macropinocytic-like uptake mechanism. Our proteomic analysis identified relevant proteins involved in nanoparticle uptake and trafficking, indicating that nanoparticles are endocytosed by a macropinocytic-like uptake mechanisms. This was underlined by the identification of ARF1, which mainly controls the uptake of nanoparticles inside this pathway. This mechanism was shown to be more dependent on classical factors of macropinocytic signaling but is also controlled by factors such as dynamin-2. Following uptake, this entry pathway guides the nanoparticles *via* macropinosome-like organelles into an endolysosomal pathway toward their final destination inside multilamellar lysosomes. The active movement of the nanoparticles inside RhoB⁺ macropinosomes and Rab7⁺/Rab9⁺ late endosomes was shown in a single-nanoparticle-tracking experiments. Besides markers for early endocytic vesicles and late endosomes, we also identified several lysosomal matrix proteins that are known for specific and unspecific degradation of cargoes.⁵² Here, knowledge about the microenvironment with which a nanoparticle is confronted is of major interest for the future design of nanocarriers. Several drug delivery applications already rely on the intravesicular milieu utilizing environmental conditions for nanomaterial disassembly and drug release.⁵⁴ However, the disassembly mechanisms of the nanospheres are nowadays more or less based on randomized strategies since the endolysosomal milieu of nanoparticles was yet undefined. We showed that the proteomic microenvironment of the endolysosome interacts with the nanoparticle resulting in the degradation of the nanoparticle-associated protein corona. Our approach may provide novel information for the intelligent design of nanospheres obtaining a high efficiency of drug release. In the future, we will transfer this technique to other cell types such as dendritic cells and macrophages to obtain further exciting insights in the uptake and trafficking pathways of nanoparticles.

MATERIAL AND METHODS

Materials. All chemicals were used without purification except for styrene, which was passed through a basic aluminum oxide before use: ammonium hydroxide (28% solution in water,

VWR), 2,2'-azobis(2-methylbutyronitrile) (V-59, Wako), ferric chloride hexahydrate ($\text{FeCl}_3 \cdot 6\text{H}_2\text{O}$, 99%, Acros), ferrous chloride tetrahydrate ($\text{FeCl}_2 \cdot 4\text{H}_2\text{O}$, 99%, Merck), *N*-(2,6-diisopropylphenyl)-perylene-3,4-dicarbonacid-imide (PMI, BASF), *n*-hexadecane

(99%, Fisher), *n*-octane (99%, Aldrich), oleic acid (58%, Riedel-de Haen), potassium persulfate (KPS, 99%, Aldrich), sodium *n*-dodecyl sulfate (SDS, 99%, Merck), sodium *p*-styrenesulfonate, (>90%, Aldrich), styrene (>99%, Aldrich). BODIPY dye was synthesized as described elsewhere.^{55,56} The used BODIPY was excited with a 514 nm laser. Emission was detected at 530–560 nm. Therefore, it was possible to perform colocalization experiments with GFP-tagged proteins since both fluorescence signals did not interfere with each other in a sequential scanning mode in cLSM experiments.

Preparation of Oleate-Capped Iron Oxide Nanoparticles. The preparation of oleate-capped iron oxide nanoparticles was performed similar to a recipe described in literature.⁵⁷ Briefly, 24.4 g (90 mmol) of ferric chloride and 12.0 g (60 mmol) of ferrous chloride were dissolved in 100 mL of deionized water. Then, 40 mL of a 28% aqueous ammonium hydroxide solution and 4.0 g (14.2 mmol) of oleic acid were added. The reaction mixture was heated to 70 °C for 1 h followed by a further heating to 100 °C at which temperature the mixture was stirred for additional 2 h under constant refilling of evaporating water. The resulting black precipitate was purified several times by magnetic separation and rinsing with deionized water and finally dried under vacuum overnight.

Preparation of Dye Labeled Polystyrene Nanoparticles with Iron Oxide Nanoparticles. The preparation of the particles was done using a modified protocol previously described.⁵⁷ Therefore, 1 g of the as-synthesized oleate-capped iron oxide nanoparticles was redispersed in 0.5 g of *n*-octane and 1 mg (2.1 μmol) of BODIPY dye added. To help redispersion and dissolving, the mixture was sonified for 45 min. In a separate vial, 25 mg of sodium dodecyl sulfate was dissolved in 24 g of deionized water, combined with the disperse *n*-octane phase and sonified with a tip sonifier for 3 min (70% amplitude, 10 s pulse, 5 s pause; Branson sonifier 450; Branson, MO) in ice. For a second emulsion, *n*-hexadecane (20 mg; 0.088 mmol) and styrene (1 g; 9.6 mmol) were mixed with a 0.04 wt % aqueous SDS solution. The two-phase system was sonified with a tip sonifier for 1 min (10% amplitude, 5 s pulse, 5 s pause) in ice and added to the magnetic miniemulsion. Nitrogen was bubbled through the combined dispersions for 5 min, KPS (25 mg; 0.092 mmol) and sodium styrenesulfonate (30 mg; 0.145 mmol) were added, and the reaction mixture was heated to 80 °C under stirring and kept at this temperature for 6 h. Purification of the magnetic polystyrene particles was performed magnetically.

Nanoparticle Characterization. Determination of the hydrodynamic particle diameter and the standard deviation was done using a NICOMP zetasizer (Agilent Technologies). The measurement was conducted at 25 °C in a diluted aqueous dispersion at an angle of 90°. Zeta potential measurements were performed with a Malvern Instruments Zeta Nanosizer at a detection angle of 173° in a 10⁻³ M KCl sample dispersion. TEM was performed using a Zeiss EM912 at a working voltage of 80 kV. The sample dispersion was diluted with demineralized water and drop-casted on a 400-mesh carbon-coated copper grid. Thermogravimetric analysis measurements were done with a thermobalance Mettler Toledo TGA/SDTA 851. All measurements were performed at a heating rate of 10 K·min⁻¹ from room temperature to 700 °C under nitrogen atmosphere. For molecular mass determination, a PSS SecSecurity (Agilent Technologies 1260 Infinity) was used. The dye labeled polymer was freeze-dried after synthesis and dissolved in DMF. Size exclusion chromatography was run at a flow rate of 1 mL·min⁻¹ and a column temperature of 30 °C. Calibration was done with polystyrene standards purchased from Polymer Standard Service GmbH (PSS). As detectors, a UV S3702 (at 520 nm) and a shodex RI 101 detector were used simultaneously. Hysteresis measurements were performed on a vibrating sample magnetometer. Samples were filled into a gelatin capsules and mounted in a low magnetic moment sample holder.

Label-Free Liquid Chromatography Mass Spectrometry. LC-MS Protein Digestion. Aliquots (20 μg) of protein were dissolved in lysis buffer (7 M urea, 2 M thiourea, 2% CHAPS). Subsequently, proteins were digested using a modified FASP method.⁵⁸ Briefly, redissolved protein was loaded on the filter, and detergents were removed by washing three times with buffer containing 8

M urea. The proteins were then reduced using dithiothreitol (DTT) and alkylated using iodoacetamide, and the excess reagent was quenched by addition of additional DTT and washed through the filters. Buffer was exchanged by washing with 50 mM NH₄HCO₃, and proteins were digested overnight by trypsin (Trypsin Gold, Promega) with an enzyme to protein ratio of 1:50. After overnight digestion, peptides were recovered by centrifugation and two additional washes using 50 mM NH₄HCO₃. Flow-throughs were combined, lyophilized and redissolved in 20 μL of 0.1% formic acid by sonification. The resulting tryptic digest solutions were diluted with aqueous 0.1% (v/v) formic acid to a concentration of 200 ng/μL and spiked with 25 fmol/μL of enolase 1 (*Saccharomyces cerevisiae*) tryptic digest standard (Waters Corporation).

UPLC-MS Configuration. Nanoscale LC separation of tryptic peptides was performed with a nanoAcuity system (Waters Corporation) equipped with a HSS-T3 1.7 μm, 75 μm × 150 mm analytical reversed-phase column (Waters Corporation). Trapping column was a Waters Symmetry C18 180 μm × 20 mm column. Then, 300 ng of total protein was injected per technical replicate. Mobile phase A was water containing 0.1% (v/v) formic acid, while mobile phase B was acetonitrile containing 0.1% (v/v) formic acid. Peptides were separated with a gradient of 5–40% mobile phase B over 94 min at a flow rate of 300 nL/min, followed by a 4 min column rinse with 90% of mobile phase B at 600 nL/min. The columns were re-equilibrated at initial conditions for 15 min. The analytical column temperature was maintained at 55 °C. The lock mass compound, [Glu¹]-Fibrinopeptide B (100 fmol/μL), was delivered by the auxiliary pump of the LC system at 500 nL/min to the reference sprayer of the NanoLockSpray source of the mass spectrometer.

Mass spectrometric analysis of tryptic peptides was performed using a Synapt G2-S mass spectrometer (Waters Corporation, Manchester, U.K.). For all measurements, the mass spectrometer was operated in v-mode with a typical resolution of at least 25 000 fwhm (full width half-maximum). All analyses were performed in positive mode ESI. The time-of-flight analyzer of the mass spectrometer was externally calibrated with a NaI mixture from *m/z* 50 to 1990. The data were postacquisition lock mass corrected using the doubly charged monoisotopic ion of [Glu¹]-Fibrinopeptide B. The reference sprayer was sampled with a frequency of 30 s. Accurate mass LC-MS data were collected in ion-mobility enhanced data-independent mode of analysis as described previously in detail.³⁰ The spectral acquisition time in each mode was 0.6 s with a 0.05-s interscan delay. In low energy MS mode, data were collected at constant collision energy of 4 eV. In elevated energy MS mode, the collision energy was ramped from 18 to 60 eV during each 0.6-s integration. One cycle of low and elevated energy data was acquired every 1.3 s. The radio frequency (RF) amplitude applied to the quadrupole mass analyzer was adjusted such that ions from *m/z* 350 to 2000 were efficiently transmitted, ensuring that any ions observed in the LC-MS data less than *m/z* 350 were known to arise from dissociations in the collision cell. All samples were analyzed in triplicate.

Data Processing and Protein Identification. Continuum LC-MS data were processed and searched using ProteinLynx GlobalSERVER version 3.0.2 (Waters Corporation). Protein identifications were obtained by searching the human UniProtKB/Swissprot reference proteome database (UniProtKB release 2012_07, 20 231 entries). Sequence information on enolase 1 (*S. cerevisiae*) and bovine trypsin was added to the databases to conduct absolute quantification.⁵⁹ Guideline identification criteria were applied for all searches.⁶⁰ For database search in PLGS3.0.2, precursor and fragment ion mass tolerances were automatically determined by PLGS3.0.2. Ion mass tolerance was typically below 5 ppm (3.3 ppm RMS) for precursor ions and below 10 ppm for fragment ions. The following search criteria were set for peptide identification: (i) trypsin as digestion enzyme, (ii) up to two missed cleavages allowed, (iii) fixed carbamidomethylcysteine and variable methionine oxidation set as the modifications, (iv) minimum three identified fragment ions. A reversed database, which was generated automatically in PLGS3.0.2, was used for the determination of the false discovery rate (FDR) for peptide and protein identification. The FDR was

set to 1% for initial database search in PLGS. Data were postprocessed using the software package ISOQuant.³⁰ Post-identification analysis included retention time alignment, EMRT (exact-mass-retention-time) and IMS clustering, signal annotation, normalization and protein isoform/homology filtering. ISOQuant filtering reduced the peptide and protein FDRs to below 0.01% and 0.1%. Only proteins identified by at least two peptides with a minimum length of six amino acids were considered. Each peptide had to be identified in a minimum of two runs. To assess protein quantities, absolute in-sample amounts were calculated for each detected protein based on the TOP3 approach.¹³ For display, we defined the relative amount of each protein in respect to the sum over all detected proteins (ppm: parts per million (w/w) of total protein). The mass spectrometry proteomics data have been deposited to the ProteomeXchange Consortium (<http://proteomecentral.proteomexchange.org>) via the PRIDE partner repository⁶¹ with the data set identifier PXD001175.

DAVID Ontology Analysis. After data evaluation of the MS spectra, >2-fold enriched proteins of the magnetic fraction were forwarded to DAVID protein ontology analysis (<http://david.abcc.ncifcrf.gov/>).⁶² Functional annotation clustering was performed using DAVID ontology analysis with the GOTERM_CC_FAT. High stringency analysis classified proteins in different annotation clusters. P-values were calculated. Reconstruction of intracellular nanoparticle trafficking is based on the GOTERMs vesicles and lysosome.

Cell Culture, Immunofluorescence, and Confocal Laser Scanning Microscopy. HeLa cells (DSMZ, Germany) were cultivated in Dulbecco's modified Eagle's medium (DMEM; Life Technologies) supplemented with 10% fetal calf serum (Invitrogen), 100 units of penicillin, 100 µg mL⁻¹ streptomycin and 1 mM pyruvate (all Life Technologies) in a humidified incubator with 5% CO₂ at 37 °C (Labotec, Germany). Human mesenchymal stem cells were cultivated in DMEM supplemented with 20% fetal calf serum (Invitrogen), 100 units of penicillin, 100 µg mL⁻¹ streptomycin and 1 mM pyruvate. Nanoparticles were added in a concentration of 150 µg mL⁻¹ for the indicated time. The indicated concentration of 150 µg mL⁻¹ was chosen because of the high yield of endosomes after their magnetic isolation. After nanoparticle incubation, cells were fixed with 4% paraformaldehyde and 0.025% glutaraldehyde for 20 min (both Sigma-Aldrich). Cell permeabilization was conducted with 0.1% saponin (Sigma-Aldrich) for 10 min at room temperature (RT). Blocking was performed by the incubation of 3% BSA for 10 min at 37 °C. The primary antibodies were incubated for 60 min in 1% BSA at 37 °C. After a wash step, the respective secondary antibody was applied for 30 min in 1% BSA at 37 °C. For the detection of lipid droplets, we used guinea pig α-TIP47 (Progen, Germany). For detection of Pmel17 after overexpression, we used a NKI/beteb antibody (Abcam). Detection of Cathepsin D, Lamp1 and Lamp2 was performed with antibodies from BD Biosciences. For immunostaining, cells were seeded in Ibidi iTreat µ-dishes at 15 000 cells cm⁻². Cells were imaged by confocal laser scanning microscopy using a commercial setup (LSM SP5 STED Leica Laser Scanning Confocal microscope, Leica Microsystems, Germany) consisting of an inverse fluorescence microscope DMI 6000 CS equipped with a laser combination and with five detectors operating in a range of 400–800 nm. A HCX PL APO CS 63×/1.4–0.6 oil objective was used. Nanoparticles (pseudocolored red) were excited with an argon laser (20 mW; λ = 514 nm) and detected at 530–545 nm. Secondary antibodies were excited with a 488 nm HeNe laser (pseudocolored green) and detected at 510–525 nm in a sequential scanning mode. Image analysis was performed with LAS AF software (Leica, Germany). **Live cell imaging:** cells were incubated with 150 µg mL⁻¹ SPIOPSN for the times as indicated. Cells were washed with DMEM and PBS and analyzed by confocal microscopy. Vesicular marker proteins were pseudocolored green, whereas SPIOPSN were pseudocolored red. Live cell imaging was performed with the XYT mode of the LAS AF software (Leica). Recording of z-Stacks was conducted in a step-size of 300 nm.

Fluorescence Activated Cell Sorting (FACS) and Inhibitor Studies. Nanoparticle uptake was quantitatively measured by fluorescence activated cell sorting (FACS). HeLa cells were

seeded at 15 000 cells cm⁻² and incubated with 150 µg mL⁻¹ magnetic nanoparticles for the respective time. Then, cells were washed with DPBS (Life Technologies), trypsinized and forwarded to FACS measurements. Flow cytometric analysis was performed using a CyFlow ML cytometer (Partec, Germany) with a 488 nm laser for the excitation of BODIPY and a 527 nm band-pass filter for emission detection. Cytotoxicity was measured staining the cells with 28.6 mg mL⁻¹ 7-aminoactinomycin D (7-AAD). Excitation of 7-AAD was conducted at 562 nm and emission was measured at 682 nm. Data analysis was performed using FCS Express V4 software (DeNovo Software) by selecting the counted cells on a forward/sideward scatter plot, thereby excluding cell debris. These events were further analyzed for uptake. Median intensity was determined in triplicates. **Inhibitor experiments:** in experiments with small molecule inhibitors, cells were pretreated for 30–45 min with the indicated concentrations of the inhibitors (Sigma-Aldrich), washed and then incubated with nanoparticles for 5 h. The solvent served as a control. The stocks of the inhibitors were at least 1000-fold concentrated and freshly prepared before the experiments. Cytochalasin D, IPA-3, Wortmannin, Ly294002, dynasore, EIPA, chlorpromazine and nocodazole (all Sigma-Aldrich) was solved in molecular grade DMSO. Methyl-*b*-cyclodextrin was dissolved in water (Sigma-Aldrich).

Transfections, Nucleofections, siRNA, and Used Plasmids/Markers. HeLa cells were transfected 24 h before adding the SPIOPSN (150 µg mL⁻¹) using the standard protocol of Fugene HD (Promega). We used a transfection agent/DNA ratio of 3:1 in all experiments. Ready to use Pmel17-pCMV6-XL5 was used for transfection (Origene). pcDNA3-EGFP-Rac1-Q61L, pcDNA3-EGFP-Cdc42-T17N was kindly provided by Gary Bokoch.⁶³ pcDNA3 HA Arf1 DN T31N was kindly provided by Thomas Roberts.⁶⁴ pcDNA3-EGFP-Cdc42(Q61L) was provided by Klaus Hahn.⁶⁵ Alpha 5 integrin-GFP was provided by Rick Horwitz.⁶⁶ Channing Der provided GFP-RhoB.⁶⁷ GFP-Rab5DN(S34N) was provided by Sergio Grinstein.⁶⁸ pEGFP VAMP7 (1–220) was provided by Thierry Galli.⁶⁹ Rab5-GFP and Rab7-GFP were provided by M. Zerial (Max Planck Institute of Molecular Cell Biology and Genetics). Dynamin2 K44A, Cav1-GFP and Epsin DIII-GFP were provided by Addgene. Transfection was performed using Fugene HD (Lonza). siRNAs were nucleofected with an Amaxa Nucleofector 4D (Lonza, Switzerland) as described by the manufacturer. Nucleofection efficiency (95–99% siRNA loading) was verified with a AF555 coupled siRNA by flow cytometry. siRNA sequences: CD82-siRNA, GCCCUCAAGGGUGUGUAUATT (Ambion); CD81-siRNA, UGAUGUUCGUUGGUUUCGUTT (Eurofins, Germany); CD9-siRNA, GGAGUCUAUUUCU-GAUCGT; CD63-siRNA, UAUGGUCUGACUAGGACAAGCUGUTT (Ambion, Germany); Flotillin-1-siRNA (Santa Cruz, sc-35391); Caveolin-1-siRNA, GCGUGUCAUUCCAUUATT (Ambion); Clathrin-HC-siRNA, UAAUCCAAUUCGAAGACCAAUTT (Eurofins); cdc42-esiRNA (Sigma-Aldrich). Negative controls were mock transfected. **Fluorescent tracer of macropinocytosis:** AF 488 dextran (10 kDa; Life technologies).

qPCR and Western Blot of Knockdowns. RNA isolation was performed 48 h after siRNA knockdown with the RNAeasy mini kit (Qiagen, Germany). cDNA synthesis was performed with iScript cDNA synthesis kit (Biorad, Germany). SYBR green supermix was used for all measurements (Biorad, Germany). The following primers were used: CD82-for, ACTGGACAGACAAC-GCTGAG; CD82-rev, GTTGTGCGAAAGACACTCT; CD81-for, CTCCAGCACACTGACTGCT; CD81-rev, TCGTTGGAGAACGTTCT; CD9-for, GCATGCTGGGACTGTCTT; CD9-rev, TAAGGGTTCTACTCCAC; CD63-for, CGAAAAAACACCACACTGCT; CD63-rev, TTAGGGGAAGGTACAGCTTC; Flotillin-1-for, GCATTG-CCCAGGTAAAATC; Flotillin-1-rev, CTTCTGCCTCCGACTCTAAC; Caveolin-1-for, GCGACCCTAACACCTGAAC; Caveolin-1-rev, TGTTGTCAAAGTGGCGTA; Clathrin-HC-for, GAGCCTCTGCT-GACATCAC; Clathrin-HC-rev, TTATTAGCGGGTAGACTTCC; GAPDH-for, AAGGTGAACGTCGAGTCAA; GAPDH-rev, GGTAGT-TACTGGGAAGTAA. (Eurofins MWG Operon, Germany). The following primers were used for ER stress measurements and DMT1 measurements: Grp94-for, TATGTGCGCCGTATTGAT and Grp94-rev, GGGGAGATCATGAGTCCA; Grp78-for, TAGTG-CAAGCTGAAGGCTGA and Grp78-rev, GGGCTGGAGTACAG

TGGTGT; Xbp-1-for, CTGGAACAGCAAGTGGTAGA and Xbp-1-rev, CTGGTC CTTCTGGGTAGAC; DMT1-for, TGAATGCCACAATACGA-AGG and DMT1-rev, ATAAAGCCACAGCCGATGA. As reference, actin-for, TCGTGCCTGACATTAAGGGG and actin-rev, GTACTTG-CGCTCAGGAGGAG were used. qPCR was performed in a Biolog CFX96 instrument and analyzed by the $\Delta\Delta Ct$ method. *Western Blot*: protein samples were blotted on PVDF membranes and analyzed with anti-CD81 (Santa Cruz, CA), anti-Clathrin HC (BD Biosciences), anti-GAPDH (Abcam), anti-Flotillin-1 (BD Biosciences), anti-CD63 (Biolegend), anti-Caveolin-1 (Santa Cruz, CA), and anti-NPC1 (Abcam).

Magnetic Separation of Vesicles. For purification of vesicles, cells were loaded with SPIOPSN. A total of $150 \mu\text{g mL}^{-1}$ of the nanoparticles was added to 1.8×10^7 HeLa cells growing in the exponential phase (DSMZ, Germany) for 20 h at 37°C and 5% CO_2 . Cells were thoroughly washed 10 times with 100 mL of PBS (Life technologies) to remove extracellular particles and debris. After the neutralization of trypsin with cell culture medium, further washes were conducted. Cell disruption was performed using a 27 G needle (BD Biosciences) during exactly 35 strokes under microscopic observation. Here, intact vesicles were released from the cytosol. This step was performed on ice and in 0.5 mL of PBS with complete protease inhibitor (Roche, Switzerland). Cell debris was removed by centrifuging the sample for 5 min at 453g at 4°C . The supernatant was re-centrifuged until no pellet was detectable. The brownish cytosolic supernatant was then injected into a custom-made magnetic sorting device with a strong neodymium magnet (Q-60-30-15-N, Supermagnete, Germany). Magnetic sorting was conducted over 12 h under cooling and in the presence of protease inhibitors over a magnetic field distance of 10 cm. The small magnetic pellet was carefully washed five times with 3 mL of PBS (with protease inhibitor). For quality control, parts of the magnetic pellet were transferred to transmission electron microscopy and checked for nonvesicular impurities. For label-free quantitative LC-MS, nanoparticle associated proteins were solubilized in 25 μL of lysis-buffer (7 M urea, 2 M thiourea, 4% CHAPS). After solubilization, nanoparticles were pelleted for 30 min at 20000g and the supernatant was forwarded to LC-MS analysis. The nonmagnetic fraction was treated comparably. *Mouse experiments*: 2 mg of SPIOPSN was tail-vain-injected into BALB/C mice ($n = 3$). After 20 h of SPIOPSN exposure, peripheral blood, spleen, liver and kidney were isolated, and single cell suspensions were obtained using a cell strainer. Cells were magnetically separated by MACS columns and forwarded to confocal microscopy for qualitative analysis.

Transmission Electron Microscopy Using High Pressure Freezing As Fixation Method. To visualize the SPIOPSN nanoparticles at high resolution in cellular environment, we applied transmission electron microscopy of HeLa cells treated with $150 \mu\text{g mL}^{-1}$ of the particles for 24 h. Before treatment, cells were left to grow for 48 h after seeding onto 3 mm Ø sapphire discs at a density of $15\,000 \text{ cells} \cdot \text{cm}^{-2}$ in a 24-well plate. At the end of the incubation period, cells were fixed by means of high pressure freezing using a Compact O1 HPF machine (Wohlgemuth GmbH, Switzerland). Subsequent freeze-substitution was conducted using a Leica EM AFS 2 device (Leica Microsystems, Germany). The substitution medium contained acetone p.a., 0.2% osmium tetroxide, 0.1% uranyl acetate and 5% water and was precooled to -90°C before samples were added. After freeze-substitution, samples were washed twice with acetone p.a. and finally embedded into EPON 812 resin. Ultrathin sectioning of the embedded samples was performed using a Leica Ultracut UCT (Leica Microsystems, Germany) and a diamond knife. Examination of thin sections was conducted using a FEI Tecnai F20 transmission electron microscope (FEI, USA) operated at an acceleration voltage of 200 kV. Bright field images were acquired using a Gatan US1000 slow scan CCD camera (Gatan, Inc.).

Conflict of Interest: The authors declare no competing financial interest.

Acknowledgment. The authors wish to thank the Deutsche Forschungsgemeinschaft (DFG, SFB1066 and SPP1313, LA1013/13-1; MA 3271/3-1) for supporting the study. The Max Planck

society is gratefully acknowledged. M.B.B. is a recipient of a fellowship funded through the Excellence Initiative (DFG/GSC 266). S.T. and H.S. were supported by Stiftung Rheinland-Pfalz (NANOSCH) and the DFG (SFB 1066). The authors have no other relevant affiliations or financial involvement with any organization or entity with a financial interest in or financial conflict with the subject matter or material discussed in the manuscript apart from those disclosed. The authors would like to thank Christoph Sieber for excellent technical assistance in sample preparation for transmission electron microscopy and Andrey Turshatov for providing us the BODIPY dye for nanoparticle synthesis. We thank Patricia Okwinka and Maria Sommer for performing the nanoparticle injection and the preparation of the samples in animal experiments.

Supporting Information Available: Cytotoxicity of nanoparticles after 20 h of exposure; colocalization with different markers; different inhibitors/stimulators and their effect on SPIOPSN uptake; overexpression and knockdown of different endocytosis-associated proteins; nanoparticles traffic inside late endosomal/lysosomal VAMP7+ vesicles; intracellular trafficking of SPIOPSN in human mesenchymal stem cells; the protein corona co-internalized with nanoparticles and then degraded inside the lysosome; analysis of *in vivo* distribution of SPIOPSN after 20 h; data for label-free quantitative mass spectrometry. This material is available free of charge via the Internet at <http://pubs.acs.org>.

REFERENCES AND NOTES

1. Treuel, L.; Brandholt, S.; Maffre, P.; Wiegele, S.; Shang, L.; Nienhaus, G. U. Impact of Protein Modification on the Protein Corona on Nanoparticles and Nanoparticle-Cell Interactions. *ACS Nano* **2014**, *8*, 503–513.
2. Tenzer, S.; Docter, D.; Kuharev, J.; Musyanovych, A.; Fetz, V.; Hecht, R.; Schlenk, F.; Fischer, D.; Kiouptsis, K.; Reinhardt, C.; et al. Rapid Formation of Plasma Protein Corona Critically Affects Nanoparticle Pathophysiology. *Nat. Nanotechnol.* **2013**, *8*, 772–781.
3. Tenzer, S.; Docter, D.; Rosfa, S.; Włodarski, A.; Kuharev, J.; Rekik, A.; Knauer, S. K.; Bantz, C.; Nawroth, T.; Bier, C.; et al. Nanoparticle Size Is a Critical Physicochemical Determinant of the Human Blood Plasma Corona: A Comprehensive Quantitative Proteomic Analysis. *ACS Nano* **2011**, *5*, 7155–7167.
4. Salvati, A.; Pitek, A. S.; Monopoli, M. P.; Prapainop, K.; Bombelli, F. B.; Hristov, D. R.; Kelly, P. M.; Aberg, C.; Mahon, E.; Dawson, K. A. Transferrin-Functionalized Nanoparticles Lose Their Targeting Capabilities When a Biomolecule Corona Adsorbs on the Surface. *Nat. Nanotechnol.* **2013**, *8*, 137–143.
5. Sahay, G.; Alakhova, D. Y.; Kabanov, A. V. Endocytosis of Nanomedicines. *J. Controlled Release* **2010**, *145*, 182–195.
6. Iversen, T. G.; Skotland, T.; Sandvig, K. Endocytosis and Intracellular Transport of Nanoparticles: Present Knowledge and Need for Future Studies. *Nano Today* **2011**, *6*, 176–185.
7. Rink, J.; Ghigo, E.; Kalaidzidis, Y.; Zerial, M. Rab Conversion as a Mechanism of Progression from Early to Late Endosomes. *Cell* **2005**, *122*, 735–749.
8. Galvez, T.; Gilleron, J.; Zerial, M.; O'Sullivan, G. A. Snapshot: Mammalian Rab Proteins in Endocytic Trafficking. *Cell* **2012**, *151*, No. 234e2.
9. Ohya, T.; Miaczynska, M.; Coskun, U.; Lommer, B.; Runge, A.; Drechsel, D.; Kalaidzidis, Y.; Zerial, M. Reconstitution of Rab- and Snare-Dependent Membrane Fusion by Synthetic Endosomes. *Nature* **2009**, *459*, 1091–1097.
10. Zeigerer, A.; Gilleron, J.; Bogorad, R. L.; Marsico, G.; Nonaka, H.; Seifert, S.; Epstein-Barash, H.; Kuchimanchi, S.; Peng, C. G.; Ruda, V. M.; et al. Rab5 Is Necessary for the Biogenesis of the Endolysosomal System *In Vivo*. *Nature* **2012**, *485*, 465–470.
11. Sonnichsen, B.; De Renzis, S.; Nielsen, E.; Rietdorf, J.; Zerial, M. Distinct Membrane Domains on Endosomes in the Recycling Pathway Visualized by Multicolor Imaging of Rab4, Rab5, and Rab11. *J. Cell Biol.* **2000**, *149*, 901–914.

12. Savina, A.; Fader, C. M.; Damiani, M. T.; Colombo, M. I. Rab11 Promotes Docking and Fusion of Multivesicular Bodies in a Calcium-Dependent Manner. *Transl. Cell Biol.* **2005**, *6*, 131–143.
13. Sandin, P.; Fitzpatrick, L. W.; Simpson, J. C.; Dawson, K. A. High-Speed Imaging of Rab Family Small Gtpases Reveals Rare Events in Nanoparticle Trafficking in Living Cells. *ACS Nano* **2012**, *6*, 1513–1521.
14. Minton, K. Membrane Dynamics: How Lysosomes Snare Autophagosomes. *Nat. Rev. Mol. Cell Biol.* **2013**, *14*, 65.
15. Tanida, I.; Minematsu-Ikeguchi, N.; Ueno, T.; Kominami, E. Lysosomal Turnover, but Not a Cellular Level, of Endogenous Lc3 Is a Marker for Autophagy. *Autophagy* **2005**, *1*, 84–91.
16. Pols, M. S.; van Meel, E.; Oorschot, V.; ten Brink, C.; Fukuda, M.; Swetha, M. G.; Mayor, S.; Klumperman, J. Hvps41 and Vamp7 Function in Direct Tgn to Late Endosome Transport of Lysosomal Membrane Proteins. *Nat. Commun.* **2013**, *4*, 1361.
17. Vercauteren, D.; Deschout, H.; Remaut, K.; Engbersen, J. F.; Jones, A. T.; Demeester, J.; De Smedt, S. C.; Braeckmans, K. Dynamic Colocalization Microscopy to Characterize Intracellular Trafficking of Nanomedicines. *ACS Nano* **2011**, *5*, 7874–7884.
18. Petters, C.; Bulcke, F.; Thiel, K.; Bickmeyer, U.; Dringen, R. Uptake of Fluorescent Iron Oxide Nanoparticles by Oligodendroglial Oln-93 Cells. *Neurochem. Res.* **2014**, *39*, 372–383.
19. Ruiz de Garibay, A. P.; Solinis Aspiazu, M. A.; Rodriguez Gascon, A.; Ganjian, H.; Fuchs, R. Role of Endocytic Uptake in Transfection Efficiency of Solid Lipid Nanoparticles-Based Nonviral Vectors. *J. Gene Med.* **2013**, *15*, 427–440.
20. Sahay, G.; Querbes, W.; Alabi, C.; Eltoukhy, A.; Sarkar, S.; Zurenko, C.; Karagiannis, E.; Love, K.; Chen, D.; Zoncu, R.; et al. Efficiency of Sirna Delivery by Lipid Nanoparticles Is Limited by Endocytic Recycling. *Nat. Biotechnol.* **2013**, *31*, 653–658.
21. Gilleron, J.; Querbes, W.; Zeigerer, A.; Borodovsky, A.; Marsico, G.; Schubert, U.; Manygoats, K.; Seifert, S.; Andree, C.; Stoter, M.; et al. Image-Based Analysis of Lipid Nanoparticle-Mediated Sirna Delivery, Intracellular Trafficking and Endosomal Escape. *Nat. Biotechnol.* **2013**, *31*, 638–646.
22. Bertoli, F.; Davies, G. L.; Monopoli, M. P.; Moloney, M.; Gun'ko, Y. K.; Salvati, A.; Dawson, K. A. Magnetic Nanoparticles to Recover Cellular Organelles and Study the Time Resolved Nanoparticle-Cell Interactome throughout Uptake. *Small* **2014**, *10*, 3307–3315.
23. Mercer, J.; Helenius, A. Gulping Rather Than Sipping: Macropinocytosis as a Way of Virus Entry. *Curr. Opin. Microbiol.* **2012**, *15*, 490–499.
24. Schnatwinkel, C.; Christoforidis, S.; Lindsay, M. R.; Uttenweiler-Joseph, S.; Wilm, M.; Parton, R. G.; Zerial, M. The Rab5 Effector Rabankyrin-5 Regulates and Coordinates Different Endocytic Mechanisms. *PLoS Biol.* **2004**, *2*, No. E261.
25. Kumari, S.; Mayor, S. Arf1 Is Directly Involved in Dynamin-Independent Endocytosis. *Nat. Cell Biol.* **2008**, *10*, 30–41.
26. D'Souza-Schorey, C.; Chavrier, P. Arf Proteins: Roles in Membrane Traffic and Beyond. *Nat. Rev. Mol. Cell Biol.* **2006**, *7*, 347–358.
27. Nakai, W.; Kondo, Y.; Saitoh, A.; Naito, T.; Nakayama, K.; Shin, H. W. Arf1 and Arf4 Regulate Recycling Endosomal Morphology and Retrograde Transport from Endosomes to the Golgi Apparatus. *Mol. Biol. Cell* **2013**, *24*, 2570–2581.
28. Wang, F.; Yu, L.; Monopoli, M. P.; Sandin, P.; Mahon, E.; Salvati, A.; Dawson, K. A. The Biomolecular Corona Is Retained During Nanoparticle Uptake and Protects the Cells from the Damage Induced by Cationic Nanoparticles until Degraded in the Lysosomes. *Nanomedicine* **2013**, *9*, 1159–1168.
29. Hofmann, D.; Mailander, V. Pharmacology of Nanocarriers on the Microscale: Importance of Uptake Mechanisms and Intracellular Trafficking for Efficient Drug Delivery. *Nanomedicine (London, U.K.)* **2013**, *8*, 321–323.
30. Distler, U.; Kuharev, J.; Navarro, P.; Levin, Y.; Schild, H.; Tenzer, S. Drift Time-Specific Collision Energies Enable Deep-Coverage Data-Independent Acquisition Proteomics. *Nat. Methods* **2014**, *11*, 167–170.
31. Huang da, W.; Sherman, B. T.; Lempicki, R. A. Systematic and Integrative Analysis of Large Gene Lists Using David Bioinformatics Resources. *Nat. Protoc.* **2009**, *4*, 44–57.
32. Quinn, K.; Brindley, M. A.; Weller, M. L.; Kaludov, N.; Kondratowicz, A.; Hunt, C. L.; Sinn, P. L.; McCray, P. B.; Stein, C. S.; Davidson, B. L.; et al. Rho Gtpases Modulate Entry of Ebola Virus and Vesicular Stomatitis Virus Pseudotyped Vectors. *J. Virol.* **2009**, *83*, 10176–10186.
33. Hasegawa, J.; Tsujita, K.; Takenawa, T.; Itoh, T. Arap1 Regulates the Ring Size of Circular Dorsal Ruffles through Arf1 and Arf5. *Mol. Biol. Cell* **2012**, *23*, 2481–2489.
34. Fujii, M.; Kawai, K.; Egami, Y.; Araki, N. Dissecting the Roles of Rac1 Activation and Deactivation in Macropinocytosis Using Microscopic Photo-Manipulation. *Sci. Rep.* **2013**, *3*, 2385.
35. Mercer, J.; Helenius, A. Virus Entry by Macropinocytosis. *Nat. Cell Biol.* **2009**, *11*, 510–520.
36. Iversen, T. G.; Frerker, N.; Sandvig, K. Uptake of Ricin-Quantum Dot Nanoparticles by a Macropinocytosis-like Mechanism. *J. Nanobiotechnol.* **2012**, *10*, 33.
37. Swanson, J. A. Shaping Cups into Phagosomes and Macropinosomes. *Nat. Rev. Mol. Cell Biol.* **2008**, *9*, 639–649.
38. Dharmawardhane, S.; Schurmann, A.; Sells, M. A.; Chernoff, J.; Schmid, S. L.; Bokoch, G. M. Regulation of Macropinocytosis by P21-Activated Kinase-1. *Mol. Biol. Cell* **2000**, *11*, 3341–3352.
39. Koyama, N.; Kashimata, M.; Sakashita, H.; Sakagami, H.; Gresik, E. W. Egf-Stimulated Signaling by Means of Pi3k, Plcgamma1, and Pkc Isozymes Regulates Branching Morphogenesis of the Fetal Mouse Submandibular Gland. *Dev. Dyn.* **2003**, *227*, 216–226.
40. Saeed, M. F.; Kolokoltsov, A. A.; Albrecht, T.; Davey, R. A. Cellular Entry of Ebola Virus Involves Uptake by a Macropinocytosis-like Mechanism and Subsequent Trafficking through Early and Late Endosomes. *PLoS Pathog.* **2010**, *6*, No. e1001110.
41. Gao, H.; Yang, Z.; Zhang, S.; Cao, S.; Shen, S.; Pang, Z.; Jiang, X. Ligand Modified Nanoparticles Increases Cell Uptake, Alters Endocytosis and Elevates Glioma Distribution and Internalization. *Sci. Rep.* **2013**, *3*, 2534.
42. Bryant, D. M.; Kerr, M. C.; Hammond, L. A.; Joseph, S. R.; Mostov, K. E.; Teasdale, R. D.; Stow, J. L. Egf Induces Macropinocytosis and Snx1-Modulated Recycling of E-Cadherin. *J. Cell Sci.* **2007**, *120*, 1818–1828.
43. Schlunck, G.; Damke, H.; Kiosses, W. B.; Rusk, N.; Symons, M. H.; Waterman-Storer, C. M.; Schmid, S. L.; Schwartz, M. A. Modulation of Rac Localization and Function by Dynamin. *Mol. Biol. Cell* **2004**, *15*, 256–267.
44. Vanlandingham, P. A.; Ceresa, B. P. Rab7 Regulates Late Endocytic Trafficking Downstream of Multivesicular Body Biogenesis and Cargo Sequestration. *J. Biol. Chem.* **2009**, *284*, 12110–12124.
45. Ganley, I. G.; Carroll, K.; Bittova, L.; Pfeffer, S. Rab9 Gtpase Regulates Late Endosome Size and Requires Effector Interaction for Its Stability. *Mol. Biol. Cell* **2004**, *15*, 5420–5430.
46. van Niel, G.; Charrin, S.; Simoes, S.; Romao, M.; Rochin, L.; Saftig, P.; Marks, M. S.; Rubinstein, E.; Raposo, G. The Tetraspanin Cd63 Regulates Escrt-Independent and -Dependent Endosomal Sorting During Melanogenesis. *Dev. Cell* **2011**, *21*, 708–721.
47. Berson, J. F.; Harper, D. C.; Tenza, D.; Raposo, G.; Marks, M. S. Pmel17 Initiates Premelanosome Morphogenesis within Multivesicular Bodies. *Mol. Biol. Cell* **2001**, *12*, 3451–3464.
48. Quast, T.; Eppler, F.; Semmling, V.; Schild, C.; Homsi, Y.; Levy, S.; Lang, T.; Kurts, C.; Kolanus, W. Cd81 Is Essential for the Formation of Membrane Protrusions and Regulates Rac1-Activation in Adhesion-Dependent Immune Cell Migration. *Blood* **2011**, *118*, 1818–1827.
49. Frolov, A.; Srivastava, K.; Daphna-Iken, D.; Traub, L. M.; Schaffer, J. E.; Ory, D. S. Cholesterol Overload Promotes

- Morphogenesis of a Niemann-Pick C (Npc)-like Compartment Independent of Inhibition of Npc1 or He1/Npc2 Function. *J. Biol. Chem.* **2001**, *276*, 46414–46421.
50. Glebov, O. O.; Bright, N. A.; Nichols, B. J. Flotillin-1 Defines a Clathrin-Independent Endocytic Pathway in Mammalian Cells. *Nat. Cell Biol.* **2006**, *8*, 46–54.
51. Kasper, J.; Hermanns, M. I.; Bantz, C.; Utech, S.; Koshkina, O.; Maskos, M.; Brochhausen, C.; Pohl, C.; Fuchs, S.; Unger, R. E.; et al. Flotillin-Involved Uptake of Silica Nanoparticles and Responses of an Alveolar-Capillary Barrier in Vitro. *Eur. J. Pharm. Biopharm.* **2012**, *84*, 275–287.
52. Schroder, B. A.; Wrocklage, C.; Hasilik, A.; Saftig, P. The Proteome of Lysosomes. *Proteomics* **2010**, *10*, 4053–4076.
53. Mizushima, N. Autophagy: Process and Function. *Genes Dev.* **2007**, *21*, 2861–2873.
54. Cauda, V.; Engelke, H.; Sauer, A.; Arcizet, D.; Brauchle, C.; Radler, J.; Bein, T. Colchicine-Loaded Lipid Bilayer-Coated 50 nm Mesoporous Nanoparticles Efficiently Induce Microtubule Depolymerization Upon Cell Uptake. *Nano Lett.* **2010**, *10*, 2484–2492.
55. Nikiforow, I.; Adams, J. r.; König, A. M.; Langhoff, A.; Pohl, K.; Turshatov, A.; Johannsmann, D. Self-Stratification During Film Formation from Latex Blends Driven by Differences in Collective Diffusivity. *Langmuir* **2010**, *26*, 13162–13167.
56. Hofmann, D.; Messerschmidt, C.; Bannwarth, M. B.; Landfester, K.; Mailander, V. Drug Delivery without Nanoparticle Uptake: Delivery by a Kiss-and-Run Mechanism on the Cell Membrane. *Chem. Commun. (London)* **2014**, *50*, 1369–1371.
57. Bannwarth, M. B.; Kazer, S. W.; Ulrich, S.; Glasser, G.; Crespy, D.; Landfester, K. Well-Defined Nanofibers with Tunable Morphology from Spherical Colloidal Building Blocks. *Angew. Chemie, Int. Ed.* **2013**, *52*, 10107–10111.
58. Wisniewski, J. R.; Zougman, A.; Nagaraj, N.; Mann, M. Universal Sample Preparation Method for Proteome Analysis. *Nat. Methods* **2009**, *6*, 359–362.
59. Patzig, J.; Jahn, O.; Tenzer, S.; Wichert, S. P.; de Monasterio-Schrader, P.; Rosfa, S.; Kuharev, J.; Yan, K.; Bormuth, I.; Bremer, J.; et al. Quantitative and Integrative Proteome Analysis of Peripheral Nerve Myelin Identifies Novel Myelin Proteins and Candidate Neuropathy Loci. *J. Neurosci.* **2011**, *31*, 16369–16386.
60. Bradshaw, R. A.; Burlingame, A. L.; Carr, S.; Aebersold, R. Reporting Protein Identification Data: The Next Generation of Guidelines. *Mol. Cell. Proteomics* **2006**, *5*, 787–788.
61. Vizcaino, J. A.; Cote, R. G.; Csordas, A.; Dianes, J. A.; Fabregat, A.; Foster, J. M.; Griss, J.; Alpi, E.; Birim, M.; Contell, J.; et al. The Proteomics Identifications (PrIDE) Database and Associated Tools: Status in 2013. *Nucleic Acids Res.* **2013**, *41*, D1063–1069.
62. Ashburner, M.; Ball, C. A.; Blake, J. A.; Botstein, D.; Butler, H.; Cherry, J. M.; Davis, A. P.; Dolinski, K.; Dwight, S. S.; Eppig, J. T.; et al. Gene Ontology: Tool for the Unification of Biology. *Nat. Genet.* **2000**, *25*, 25–29.
63. Subauste, M. C.; Von Herrath, M.; Benard, V.; Chamberlain, C. E.; Chuang, T. H.; Chu, K.; Bokoch, G. M.; Hahn, K. M. Rho Family Proteins Modulate Rapid Apoptosis Induced by Cytotoxic T Lymphocytes and Fas. *J. Biol. Chem.* **2000**, *275*, 9725–9733.
64. Furman, C.; Short, S. M.; Subramanian, R. R.; Zetter, B. R.; Roberts, T. M. Def-1/Asap1 Is a Gtpase-Activating Protein (Gap) for Arf1 That Enhances Cell Motility through a Gap-Dependent Mechanism. *J. Biol. Chem.* **2002**, *277*, 7962–7969.
65. Nalbant, P.; Hodgson, L.; Kraynov, V.; Toubchkin, A.; Hahn, K. M. Activation of Endogenous Cdc42 Visualized in Living Cells. *Science* **2004**, *305*, 1615–1619.
66. Laukaitis, C. M.; Webb, D. J.; Donais, K.; Horwitz, A. F. Differential Dynamics of Alpha 5 Integrin, Paxillin, and Alpha-Actinin During Formation and Disassembly of Adhesions in Migrating Cells. *J. Cell Biol.* **2001**, *153*, 1427–1440.
67. Roberts, P. J.; Mitin, N.; Keller, P. J.; Chenette, E. J.; Madigan, J. P.; Currin, R. O.; Cox, A. D.; Wilson, O.; Kirschmeier, P.; Der, C. J. Rho Family Gtpase Modification and Dependence on Caax Motif-Signaled Posttranslational Modification. *J. Biol. Chem.* **2008**, *283*, 25150–25163.
68. Bohdanowicz, M.; Balkin, D. M.; De Camilli, P.; Grinstein, S. Recruitment of Ocrl and Inpp5b to Phagosomes by Rab5 and Appl1 Depletes Phosphoinositides and Attenuates Akt Signaling. *Mol. Biol. Cell* **2012**, *23*, 176–187.
69. Martinez-Arca, S.; Alberts, P.; Zahraoui, A.; Louvard, D.; Galli, T. Role of Tetanus Neurotoxin Insensitive Vesicle-Associated Membrane Protein (Ti-Vamp) in Vesicular Transport Mediating Neurite Outgrowth. *J. Cell Biol.* **2000**, *149*, 889–900.